

The targeted delivery of multicomponent cargos to cancer cells by nanoporous particle-supported lipid bilayers

Carlee E. Ashley^{1*}†, Eric C. Carnes², Genevieve K. Phillips³, David Padilla¹, Paul N. Durfee⁴, Page A. Brown⁵, Tracey N. Hanna⁶, Juewen Liu^{1†}, Brandy Phillips³, Mark B. Carter³, Nick J. Carroll², Xingmao Jiang¹, Darren R. Dunphy¹, Cheryl L. Willman^{3,7}, Dimiter N. Petsev², Deborah G. Evans⁵, Atul N. Parikh⁸, Bryce Chackerian^{3,4}, Walker Wharton^{3,7}, David S. Peabody^{3,4} and C. Jeffrey Brinker^{1,2,3,4,9*}

Encapsulation of drugs within nanocarriers that selectively target malignant cells promises to mitigate side effects of conventional chemotherapy and to enable delivery of the unique drug combinations needed for personalized medicine. To realize this potential, however, targeted nanocarriers must simultaneously overcome multiple challenges, including specificity, stability and a high capacity for disparate cargos. Here we report porous nanoparticle-supported lipid bilayers (protocells) that synergistically combine properties of liposomes and nanoporous particles. Protocells modified with a targeting peptide that binds to human hepatocellular carcinoma exhibit a 10,000-fold greater affinity for human hepatocellular carcinoma than for hepatocytes, endothelial cells or immune cells. Furthermore, protocells can be loaded with combinations of therapeutic (drugs, small interfering RNA and toxins) and diagnostic (quantum dots) agents and modified to promote endosomal escape and nuclear accumulation of selected cargos. The enormous capacity of the high-surface-area nanoporous core combined with the enhanced targeting efficacy enabled by the fluid supported lipid bilayer enable a single protocell loaded with a drug cocktail to kill a drug-resistant human hepatocellular carcinoma cell, representing a 10⁶-fold improvement over comparable liposomes.

Targeted delivery of drugs encapsulated within nanocarriers^{1,2} can overcome problems exhibited by conventional ‘free’ drugs, including poor solubility, limited stability, rapid clearing and, in particular, lack of selectivity, which results in nonspecific toxicity to normal cells³ and prevents the dose escalation necessary to eradicate malignant cells⁴. Passive targeting schemes rely on the enhanced permeability of tumour vasculature and the decreased draining efficacy of tumour lymphatics (the so-called enhanced permeability and retention effect^{5,6}) to direct accumulation of nanocarriers at tumour sites, but the lack of cell-specific interactions needed to induce nanocarrier internalization decreases therapeutic efficacy and can result in drug expulsion and induction of multiple drug resistance (MDR; ref. 7). Furthermore, not all tumours exhibit the enhanced permeability and retention effect^{5,6}, and passively targeted nanocarriers are no more effective at treating blood cancers than free drugs⁸. Selective targeting strategies employ ligands that specifically interact with receptors expressed on the cell surface of interest to promote nanocarrier binding and internalization⁹. This strategy requires that receptors are highly overexpressed by cancer cells (10⁴–10⁵ copies/cell)

relative to normal cells to maximize selectivity and therapeutic efficacy¹. Multiple copies of a targeting ligand can be conjugated to the nanocarrier surface to promote multivalent binding effects¹⁰, which result in enhanced affinity¹¹ and more efficient drug delivery through receptor-mediated internalization pathways that help circumvent MDR efflux mechanisms¹². However, high ligand densities can promote nonspecific interactions with endothelial and other non-cancerous cells and increase immunogenicity, resulting in opsonization-mediated clearance of nanocarriers¹³. Modifying the nanocarrier surface with hydrophilic polymers, such as polyethylene glycol (PEG), increases circulation times by reducing interactions with serum proteins and mitigating uptake by phagocytic cells; such strategies invariably reduce targeting specificity, however¹³. The main challenge for targeted nanocarriers is to simultaneously achieve high targeting specificity and delivery efficiency, while avoiding nonspecific binding and entrapment by the body’s defences.

Here we report a new class of nanocarrier that synergistically combines features of mesoporous silica particles^{14–19} and liposomes^{20–22} to address the multiple challenges of targeted

¹Center for Micro-Engineered Materials, University of New Mexico, Albuquerque, New Mexico 87131, USA, ²Department of Chemical and Nuclear Engineering, University of New Mexico, Albuquerque, New Mexico 87131, USA, ³Cancer Research and Treatment Center, University of New Mexico, Albuquerque, New Mexico 87131, USA, ⁴Department of Molecular Genetics and Microbiology, University of New Mexico, Albuquerque, New Mexico 87131, USA, ⁵Department of Chemistry, University of New Mexico, Albuquerque, New Mexico 87131, USA, ⁶Department of Chemical Engineering, University of Florida, Gainesville, Florida 32611, USA, ⁷School of Medicine, Department of Pathology, University of New Mexico, Albuquerque, New Mexico 87131, USA, ⁸Department of Applied Science, University of California Davis, Davis, California 95616, USA, ⁹Self-Assembled Materials Department, Sandia National Laboratories, Albuquerque, New Mexico 87185-1349, USA. †Present addresses: Harry S. Truman Post-Doctoral Fellow; Biotechnology and Bioengineering Department, Sandia National Laboratories, Livermore, California 94551, USA (C.E.A.); Department of Chemistry, University of Waterloo, Waterloo, Ontario, N2L 3G1, Canada (J.L.). *e-mail: ceashle@sandia.gov; cjbrink@sandia.gov.

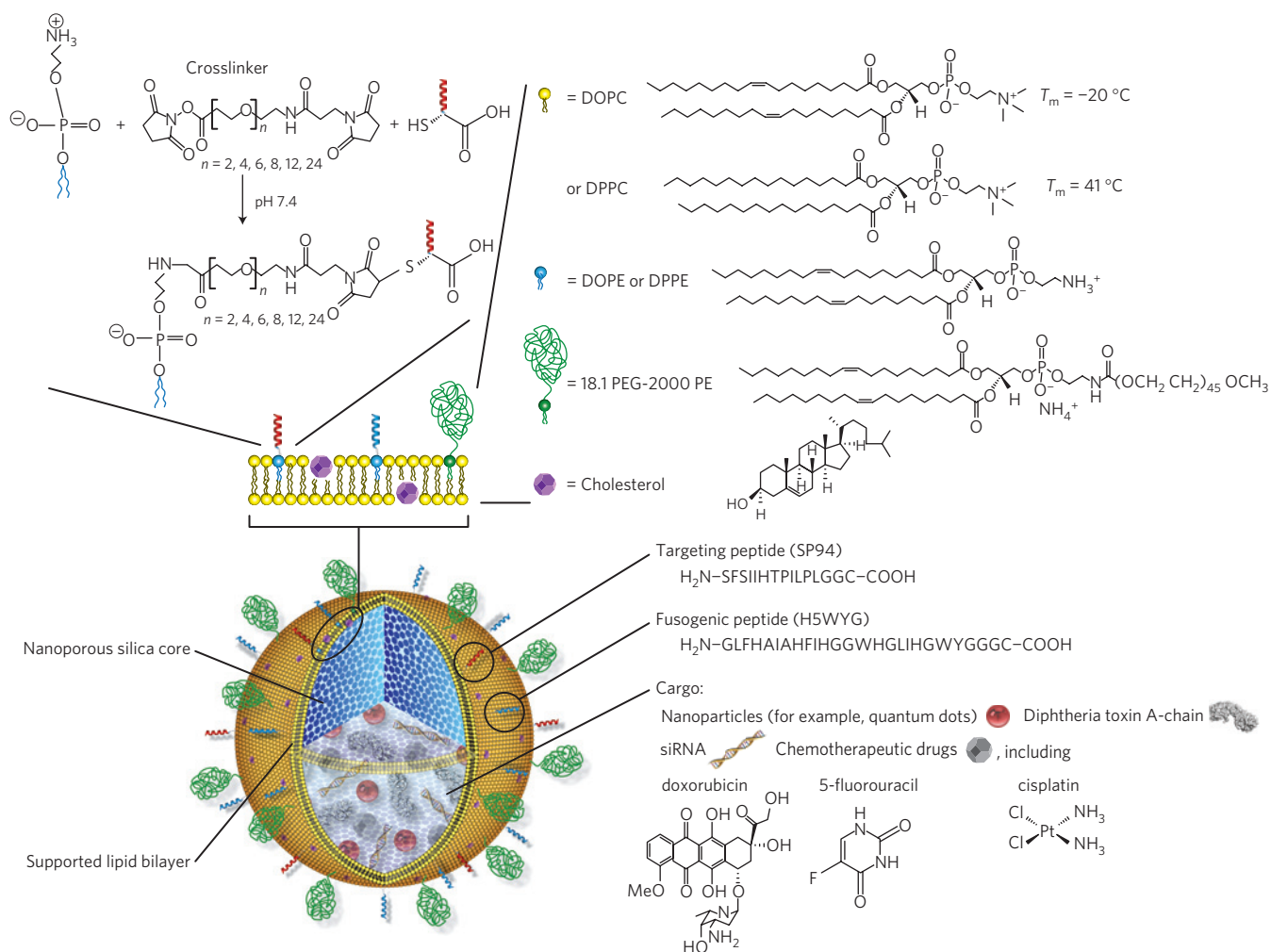


Figure 1 | Schematic illustration of the nanoporous particle-supported lipid bilayer, depicting the disparate types of therapeutic and diagnostic agent that can be loaded within the nanoporous silica core, as well as the ligands that can be displayed on the surface of the SLB. Targeting and fusogenic peptides are chemically conjugated to phosphatidylethanolamine (DOPE or DPPE), present in the SLB at 1–5 wt%, by a heterobifunctional crosslinker with a PEG spacer arm ($n = 24$). The SLB, composed of either fluid (DOPC) or non-fluid (DPPC) zwitterionic phosphatidylcholine lipids with 30 wt% cholesterol, is further modified with 5 wt% PEG-2000 PE to enhance colloidal stability and decrease nonspecific interactions.

delivery. Fusion of liposomes to a spherical, high-surface-area, nanoporous silica core^{23–26}, followed by modification of the resulting supported lipid bilayer (SLB) with multiple copies of a targeting peptide, a fusogenic peptide and PEG results in a nanocarrier construct (the ‘protocell’) that, compared with liposomes, the most extensively studied class of nanocarriers^{20–22}, improves on capacity, selectivity and stability and enables targeted delivery and controlled release of high concentrations of multicomponent cargos within the cytosol of cancer cells (see Fig. 1 and Supplementary Methods for experimental details). Specifically, owing to its high surface area ($>1,000\text{ m}^2\text{ g}^{-1}$), the nanoporous silica core (Fig. 2a) possesses a higher capacity for therapeutic and diagnostic agents than similarly sized liposomes. Furthermore, owing to substrate–membrane adhesion energy, the core suppresses large-scale bilayer fluctuations (see Supplementary Fig. S3a and refs 27–32), resulting in greater stability than unsupported liposomal bilayers. Interestingly, the nanoporous support also results in enhanced lateral bilayer fluidity compared with that of either liposomes or SLBs formed on non-porous particles. As we shall demonstrate, this synergistic combination of materials and biophysical properties enables high delivery efficiency and enhanced targeting specificity with a minimal number of targeting ligands, features crucial to maximizing specific

binding, minimizing nonspecific binding, reducing dosage and mitigating immunogenicity.

Protocells are synthesized by liposome fusion to high-surface-area spherical silica particles characterized by an isotropic, worm-like nanoporosity (see Fig. 2a and Supplementary Fig. S1). To demonstrate that SLBs formed on particles with surface-accessible nanopores have unique long-range fluidity, we carried out temperature-dependent fluorescence recovery after photobleaching (FRAP) of DPPC bilayers supported on either a nanoporous or solid (that is non-porous) silica particle (see Fig. 2b). We observe that fluorescence in the photobleached region begins to recover abruptly at $35\text{ }^\circ\text{C}$ ($\pm 1\text{ }^\circ\text{C}$) for the SLB formed on a nanoporous particle, as compared with $41\text{ }^\circ\text{C}$ ($\pm 1\text{ }^\circ\text{C}$) for the SLB formed on a solid particle; $41\text{ }^\circ\text{C}$ is the gel-to-fluid transition temperature (T_m) of DPPC, as well as the T_m reported for unilamellar DPPC liposomes³³. These data indicate that the nanoporous support results in a substantial reduction ($6\text{ }^\circ\text{C}$) in T_m . We reason that this melting-point suppression and the resulting enhancement in bilayer fluidity, also observed for nanoporous particle-supported DOPC bilayers (see Supplementary Fig. S3b), are consequences of unique physical constraints that exist at the interface between the bilayer and the nanoporous support. The underlying three-dimensional porosity and corresponding periodic roughness of the particle surface, which is composed of

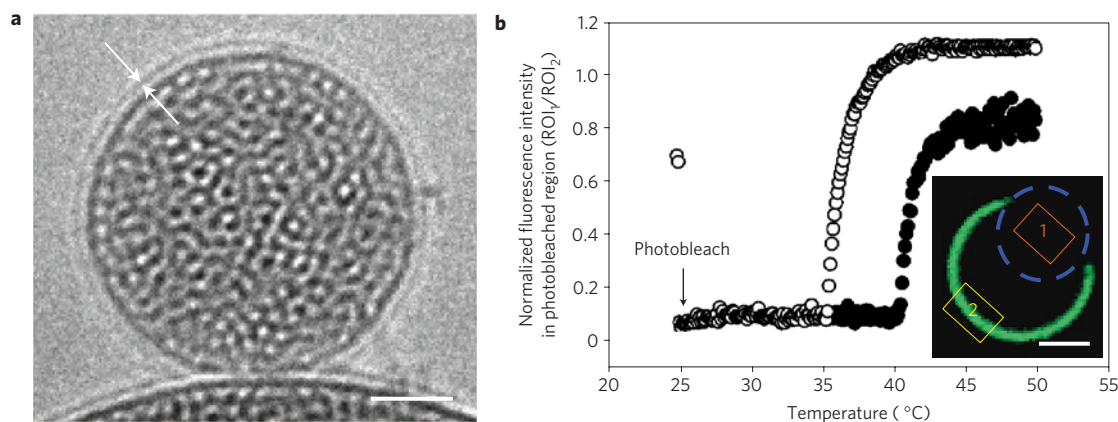


Figure 2 | Physical and biophysical characteristics of protocells. **a**, Cryogenic TEM image of the protocell, showing the nanoporous core and the SLB (~ 4 nm thick). Particle sizes reflect those naturally generated by the aerosol-assisted self-assembly process²⁶; particles were separated into a narrow distribution centred around ~ 100 nm for all surface-binding, internalization and delivery experiments (see Supplementary Fig. S1). Scale bar = 25 nm. **b**, Temperature-dependent FRAP of nitrobenzoxadiazole-labelled DPPC bilayers (green) supported on nanoporous (open circles) or solid (filled circles) spherical silica particles. Inset: normalized fluorescence recovery in the photobleached region (blue circle) was determined by dividing the fluorescence intensity in region of interest 1 (ROI₁) by the fluorescence intensity in ROI₂ to account for photobleaching that occurred during the recovery period. Scale bar = 5 μ m.

nanoscopic patches of silica and water, generate localized, nanoscale gradients in adhesion and lateral tension that enhance long-range, in-plane fluidity without introducing roughness or appreciably changing the SLB's average packing density (determined by us previously by neutron reflectivity of lipid bilayers supported on planar nanoporous supports³⁴). This conclusion is reinforced by previous experimental and theoretical studies, which found that the support suppresses all but nanoscopic, out-of-plane bilayer fluctuations^{35,36}, as well as small-angle neutron scattering data, which indicate that the protocell SLB perfectly conforms to the underlying nanoporous silica support (see Supplementary Fig. S3a). Furthermore, on the basis of simple thermodynamic arguments, we expect particle curvature to influence bilayer fluidity only for $R \ll (\kappa/2\varepsilon)^{1/2}$, where R is the particle radius, κ is the bending modulus and ε is the adhesion energy. Given that $\kappa = 10^{20}$ J for DOPC or DPPC and $\varepsilon = 10^{-3}$ – 10^{-5} J m⁻², this condition is only met when $R \ll 100$ nm, as demonstrated by recent studies that report very slight increases in the fluidity of bilayers supported on nanowires less than 50 nm in diameter³⁷. Overall, our data provide experimental evidence for previous theoretical predictions of the effect that nanoscale topography has on supported bilayer conformations^{32,38}. As described below, the enhanced fluidity of nanoporous particle-supported lipid bilayers enables protocells modified with a minimal number of targeting peptides to selectively bind to and become internalized by cancer cells, whereas their enhanced stability vis-à-vis liposomes prevents drug leakage on exposure to simulated body fluids.

The schematic diagram in Fig. 3 depicts the mechanism by which targeted protocells deliver encapsulated cargo specifically to a cancer cell of interest; successive steps of binding (step 1), internalization (step 2), endosomal escape (step 3) and nuclear targeting of desired cargo(s) (step 4) are individually described below. Protocells are synthesized by fusion of liposomes to spherical, nanoporous silica cores (100–150 nm in diameter after size separation; see Figs. 1, 2a and Supplementary Fig. S1a,d) that are preloaded by simple immersion in a solution of the desired cargo. On the basis of optimization studies (see Supplementary Fig. S5) that aimed to maximize colloidal stability and cargo retention in simulated body fluids and minimize nonspecific interactions with serum proteins and non-cancerous cells, we used the following SLB composition in all surface-binding, internalization and cargo delivery experiments: DOPC (or DPPC) with 5 wt% DOPE (or DPPE), 30 wt% cholesterol and 5 wt% 18:1

(or 16:0) PEG-2000 PE (see Fig. 1 and Supplementary Fig. S4 for lipid structures). Using a heterobifunctional crosslinker with a PEG ($n = 24$) spacer, SP94 peptides (H₂N-SFSIILTPILPLGGC-COOH, identified by filamentous phage display to have an affinity for unknown receptor(s) expressed by human hepatocellular carcinoma (HCC); ref. 39) were covalently conjugated to DOPE (or DPPE) moieties in the SLB (see Fig. 1) at concentrations ranging from 0.002 wt% (one peptide per particle, on average) to 5.0 wt% (2,048 peptides per particle, on average—see Supplementary Table S1). 120 nm liposomes with identical bilayer compositions were synthesized for comparative purposes.

Dissociation constants (K_d , where K_d is inversely related to affinity) were used to quantify surface binding of SP94-targeted protocells and liposomes to HCC cells (Hep3B), normal hepatocytes, endothelial cells and immune cells. All K_d values were determined at 4 °C to prevent nanocarrier internalization (see Supplementary Fig. S6 and Supplementary Methods). Figure 4a,b plot K_d values of SP94-targeted protocells and liposomes for Hep3B and hepatocytes as a function of average peptide density. Protocells with SLBs composed largely of DOPC (in a fluid state at 4 °C) have a high specific affinity ($K_d < 1$ nM) for Hep3B, and, over the range of 6–2,048 peptides per particle, their K_d values are consistently low (0.94–0.08 nM) and relatively independent of peptide density. This trend is not observed for DOPC liposomes, where K_d values strongly depend on peptide density and are more than ten times greater than those of comparable DOPC protocells. Similarly, protocells and liposomes with bilayers composed of DPPC (in a gel-like state at 4 °C) have K_d values that are more than ten times greater than corresponding DOPC protocells and exhibit a strong dependence on peptide density. We attribute the ability of DOPC protocells to bind to HCC with high affinity at low peptide densities to recruitment of multiple SP94 peptides to the cancer cell surface. Peptide recruitment is enabled by the fluid SLB and promotes multivalent interactions between the protocell and the target cancer cell. For DPPC protocells and liposomes, multivalent binding and correspondingly high specific affinity can only be realized at high peptide densities because non-fluid bilayers impose kinetic constraints on the lateral mobility of targeting peptides. The importance of SLB fluidity in promoting the peptide recruitment process is vividly illustrated in Fig. 4c. DOPC or DPPC liposomes were fused to planar nanoporous substrates (with a three-dimensional pore structure comparable to that of the protocell

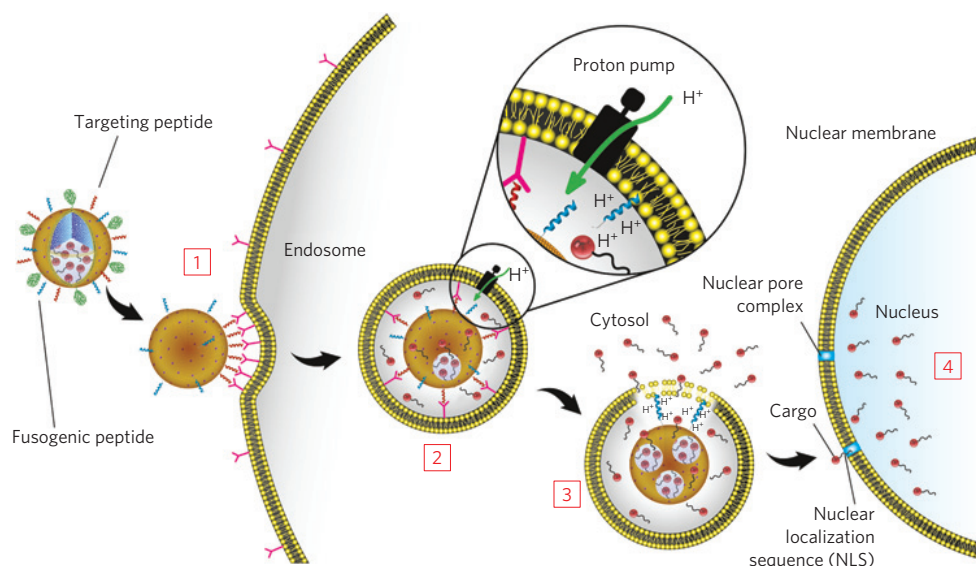


Figure 3 | Schematic diagram depicting the successive steps of multivalent binding and internalization of targeted protocells, followed by endosomal escape and nuclear localization of protocell-encapsulated cargo. DOPC protocells (1) bind to HCC with high affinity owing to recruitment of SP94 targeting peptides (magenta) to the cell surface, (2) become internalized by receptor-mediated endocytosis and (3) release their cargo into the cytosol on endosome acidification and protonation of the H5WYG fusogenic peptide (blue). (4) Cargos modified with an NLS are transported through the nuclear pore complex and become concentrated in the nucleus.

core^{40,41}), and the resulting SLBs were modified with a low density (~ 0.015 wt%, equivalent to ~ 6 peptides/particle) of SP94 peptides. On addition of Hep3B to the supported planar bilayers, we observed rapid recruitment of SP94 to the cancer cell surface when peptides were displayed on a fluid SLB but no measurable recruitment when peptides were displayed on a non-fluid SLB. This result explains the 100-fold lower K_d value of DOPC protocells versus DPPC protocells, when both display ~ 6 peptides per particle (see Fig. 4a and the following discussion).

The ability of targeting peptides, when displayed in low densities on a fluid SLB, to be recruited and multivalently bind to surface receptor(s) is crucial to enhance specific affinity, reduce nonspecific interactions and direct receptor-mediated endocytosis of nanocarriers, all of which maximize selective delivery of cargo. Concerning this point, it is important to note the influence of bilayer fluidity and stability on the peptide-density-dependent affinity of SP94-targeted protocells and liposomes for HCC (Fig. 4a) and normal hepatocytes (Fig. 4b). Non-fluid DPPC protocells and liposomes have a low affinity ($K_d \geq 1 \mu\text{M}$) for hepatocytes at high SP94 densities. However, their affinity for Hep3B ($K_d = 1\text{--}100 \text{ nM}$) is substantially lower than that of DOPC protocells ($K_d < 1 \text{ nM}$) at all peptide densities, and their K_d values for Hep3B increase more rapidly with decreasing peptide density. DOPC protocells and liposomes have similar affinities for hepatocytes at all SP94 densities (see Fig. 4b), but the K_d values of DOPC liposomes for Hep3B are between 10 and 200 times greater than those of DOPC protocells modified with the same number of peptides (see Fig. 4a). We attribute these observations to the enhanced fluidity of nanoporous particle-supported DOPC bilayers, which enables multivalent peptide recruitment to the Hep3B surface, combined with the ability of the nanoporous core to suppress the large-scale bilayer fluctuations that, for DOPC liposomes especially, seem to act as a steric barrier to high-avidity binding. The result is that DOPC protocells modified with about six copies of the SP94 peptide have a differential K_d value (HCC/hepatocytes) of 2.25×10^4 , which exceeds that of SP94-targeted DPPC protocells, DPPC liposomes and DOPC liposomes by more than 10^2 . DOPC protocells, additionally, have a 10^4 -fold higher affinity for HCC than for other control cells, including human endothelial cells, mononuclear cells,

B lymphocytes and T lymphocytes (see Supplementary Fig. S7). Also, the K_d value of DOPC protocells for Hep3B is 200 times lower than that of free SP94 for Hep3B and nearly 50,000 times lower than that of unmodified protocells for Hep3B (see Supplementary Fig. S7). If sub-nanomolar affinity is undesirable (results in reduced tumour penetration, for example), the K_d values of SP94-targeted protocells can be precisely modulated by incorporating various amounts of fluid and non-fluid lipids into the SLB (see Supplementary Fig. S8).

DOPC protocells are uniquely able to target HCC at low peptide densities, and their dramatic differential affinity for HCC translates into selective internalization when the experimental temperature is raised from 4 to 37 °C. DOPC protocells modified with a low density of SP94 peptides (~ 0.015 wt%) are efficiently endocytosed by Hep3B but not by hepatocytes, as demonstrated by the representative confocal fluorescence microscopy images shown in Fig. 4d,e; see also Supplementary Table S2, which lists average numbers of SP94-targeted protocells and liposomes internalized by Hep3B and hepatocytes. The efficacy with which targeted protocells are internalized by Hep3B depends largely on binding affinity, which can be modulated by changing bilayer fluidity and ligand density. However, it also depends on nanocarrier size (see Supplementary Fig. S9), with 50 nm protocells being most efficiently internalized ($\sim 1,800$ particles/cell). This result provides evidence that internalization occurs through an endocytotic pathway, given that membrane wrapping occurs most efficiently for particles 30–60 nm in diameter¹¹. Despite this observation, we use protocells 100–150 nm in diameter for targeted delivery, because the increased cargo capacity, which we measure to be proportional to the cube of the particle radius, more than compensates for the slightly reduced internalization efficiency.

To demonstrate that high-affinity surface binding followed by receptor-mediated endocytosis enables targeted delivery of multicomponent cargos, we loaded four fluorescently labelled surrogates, similar in size and charge to common therapeutic and diagnostic agents, within the protocell core. Figure 5a shows simultaneous encapsulation of a low-molecular-weight drug mimic (calcein), a small interfering RNA (siRNA) mimic (double-stranded DNA, dsDNA), a protein toxin mimic (red fluorescent protein,

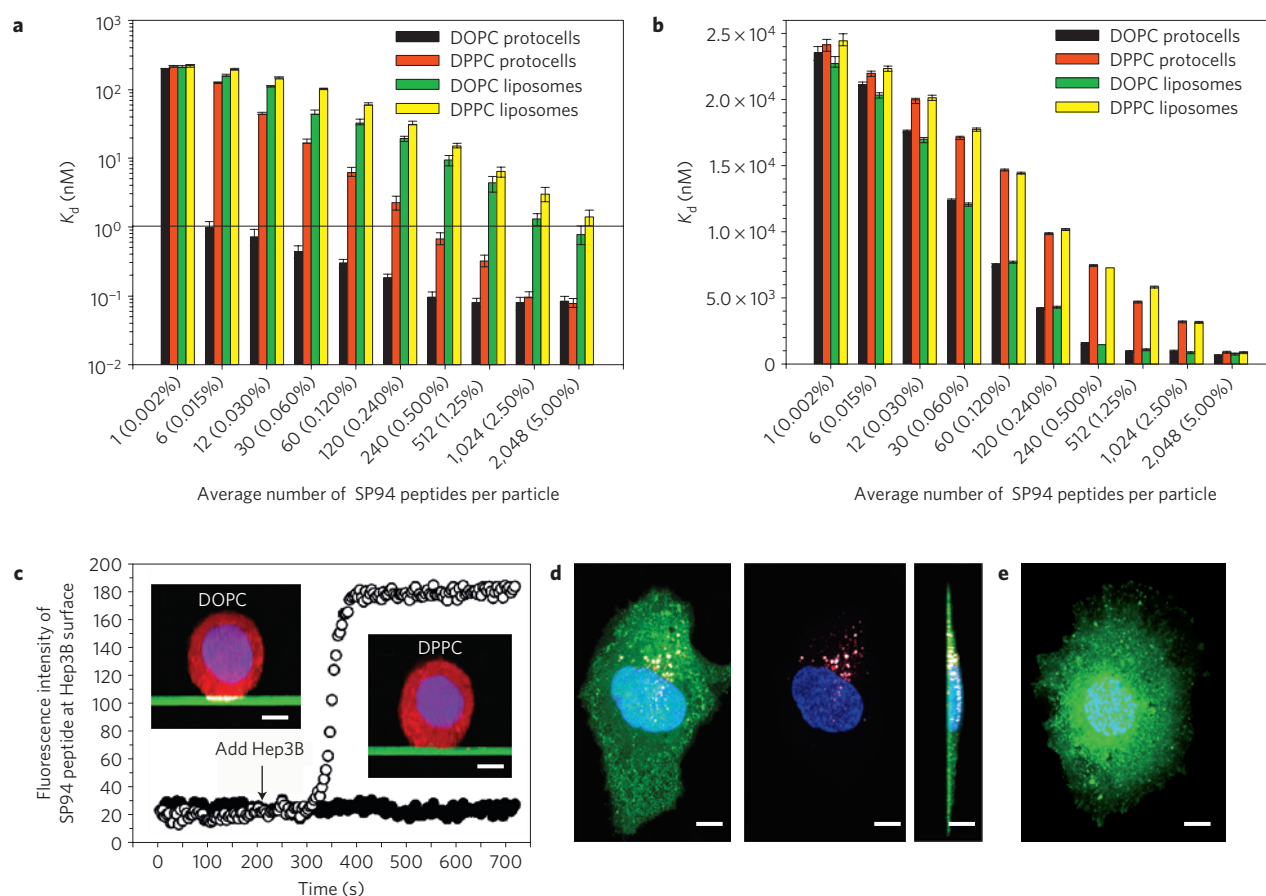


Figure 4 | Selective binding and internalization characteristics of SP94-targeted protocells. **a, b**, Dissociation constants (K_d) of SP94-targeted protocells and liposomes for Hep3B (**a**) and hepatocytes (**b**) as a function of the average number of SP94 peptides per particle (average SP94 wt% is in parentheses). All surface-binding experiments were conducted at 4 °C to prevent internalization of targeted protocells and liposomes. All error bars in **a** and **b** represent 95% confidence intervals (1.96σ) for $n = 5$. **c**, Recruitment of Alexa Fluor 647-labelled SP94 peptides (white) to the surface of a Hep3B cell when peptides are displayed on a nitrobenzoxadiazole-labelled SLB (green) composed of DOPC (open circles) or DPPC (closed circles). These data were collected at 4 °C to replicate the conditions used to determine K_d values in **a** and **b**. Hep3B cells were labelled with CellTracker Red CMTPX (red) and Hoechst 33342 (blue). Inset scale bars = 5 μm . **d, e**, Confocal fluorescence microscopy images of Hep3B (**d**) and hepatocytes (**e**) incubated with SP94-targeted protocells for 1 hour at 37 °C. Protocells were prepared with Texas Red-labelled DHPE (red) and Alexa Fluor 647-labelled nanoporous cores (white); cells were stained with CellTracker Green CMFDA (green) and Hoechst 33342 (blue). Cells shown in **d** and **e** are representative of the entire cell population (see Supplementary Table S2 for population-based internalization data); single cells were selected to enable three-dimensional imaging. Plan (left and centre images) and cross-sectional (right image) views of the three-dimensional projection are shown for **d**, whereas the plan view alone is shown for **e**. For **d**, the merged plan view (left) is shown without the green channel (centre) to enable better visualization of lipid (red) and silica (white) moieties. It is important to note that plan views of collapsed projections superimpose all slices in the z direction, giving the misleading appearance of protocells in the nucleus of **d**; this is not the case, however, as is evident in an orthogonal view of the projection (image not shown). All scale bars = 10 μm .

RFP) and a model nanoparticle (water-soluble CdSe/ZnS quantum dots), all within a fluorescently labelled porous silica particle that is completely encased in a fluorescently labelled DOPC bilayer; a protocell 10 μm in diameter was employed in this experiment to enable optical imaging. The confocal slice ($z = 5 \mu\text{m}$) demonstrates that the multiple cargos are uniformly distributed throughout the silica core and that the SLB is intact and coherent.

As illustrated schematically in Fig. 3 and confirmed by hyperspectral confocal fluorescence microscopy (Fig. 5b–d), delivery of encapsulated cargo to HCC using SP94-targeted DOPC protocells is achieved by the following successive steps. (1) Multivalent binding of SP94 to HCC surface receptor(s) initiates receptor-mediated endocytosis, an internalization pathway that helps to circumvent MDR (ref. 42). Peptide recruitment to the cell surface promotes the multivalent effects that enhance specificity. (2) As shown by the appearance of punctuate regions containing co-localized lipid, silica and cargo in Fig. 5b, protocells are rapidly endocytosed (half-life $t_{1/2} = 15 \text{ min}$) by Hep3B cells and reach a

satürating intracellular concentration (~500 protocells per Hep3B cell; see Supplementary Table S2) within an hour. Given that the SP94 peptide directs protocells to lysosomes on endocytosis by Hep3B (see Supplementary Fig. S10), we further modified the SLB with 0.500 wt% of a histidine-rich fusogenic peptide (H5WYG, $\text{H}_2\text{N}-\text{GLFHAI AHFIHGGWHGLIHGWYGGGC}-\text{COOH}$; ref. 43), which, in addition to preventing degradation of sensitive cargos in endolysosomes, promotes endosomal escape of protocells and cytosolic dispersion of encapsulated cargos (see Supplementary Fig. S11). (3) Endosome acidification destabilizes the SLB (see Supplementary Fig. S12), enabling encapsulated cargo to diffuse out of the nanoporous core. Additionally, protonation of imidazole moieties ($pK_a = 6.0$) in the fusogenic peptide initiates osmotic swelling and membrane destabilization of endosomes through the ‘proton sponge’ mechanism⁴⁴. As shown in Fig. 5c, these events enable the four surrogate cargos, along with lipid and silica moieties of the protocell, to become distributed throughout the cytosol within 4 h. (4) Cargos modified with a nuclear localization

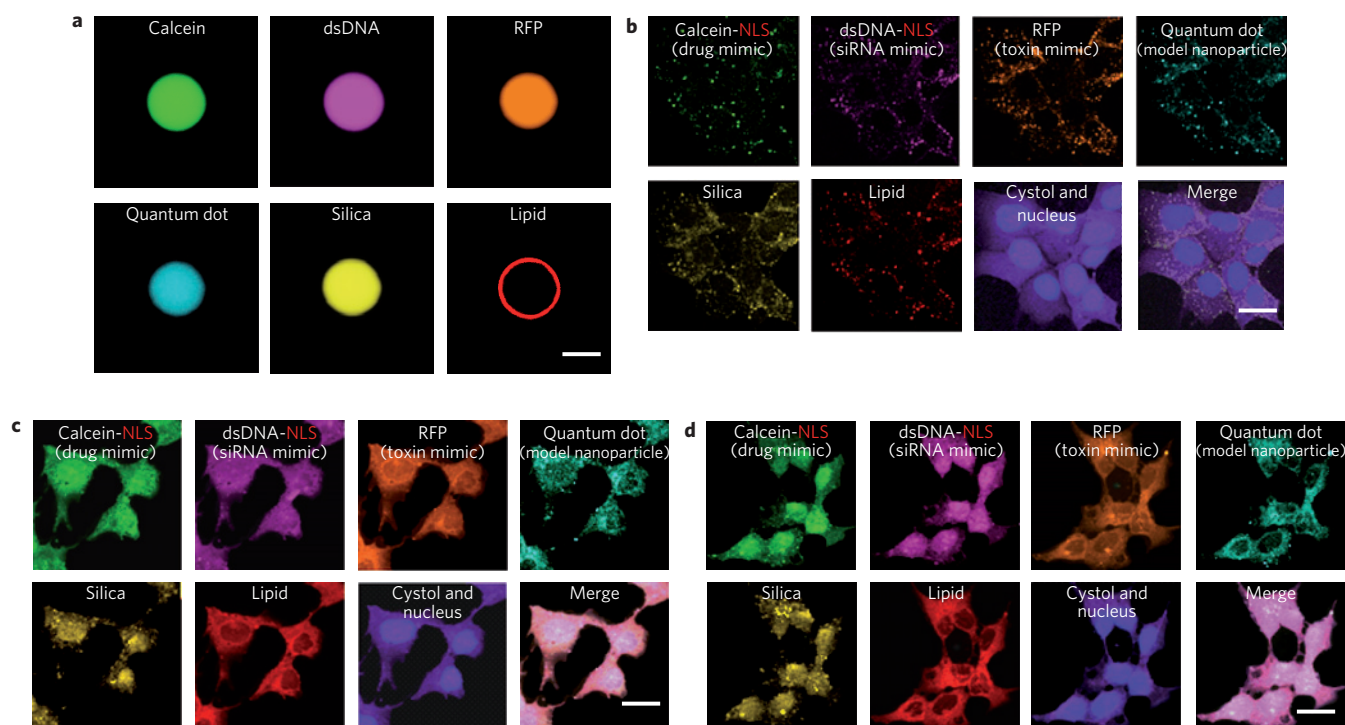


Figure 5 | Targeted delivery of multicomponent cargos to the cytosol and nuclei of HCC cells. a–d, Alexa Fluor 532-labelled nanoporous silica cores (yellow) were loaded with a multicomponent mixture of four surrogate cargos: calcein (green), an Alexa Fluor 647-labelled dsDNA oligonucleotide (magenta), RFP (orange) and CdSe/ZnS quantum dots (teal). Cargos were sealed in the cores by fusion of Texas Red-labelled DOPC liposomes (red) that contained 30 wt% cholesterol and 5 wt% PEG-2000 PE, and the resulting SLBs were modified with 0.015 wt% SP94 and 0.500 wt% H5WYG. Protocells were incubated with Hep3B cells (labelled with CellTracker Violet BMQC and Hoechst 33342) for 15 min, 4 h or 12 h (respectively) at 37 °C to collect the images shown in **b–d**. **a**, Hyperspectral confocal fluorescence microscopy slice ($z \approx 5 \mu\text{m}$) of a 10 μm protocell, demonstrating uniform loading of the nanoporous silica core and complete encapsulation of the core and cargos within the SLB. Particles 100 times larger than those used for all surface-binding, internalization and delivery studies were used in this experiment to enable optical imaging and have a 2.5×10^5 times higher capacity for the multicomponent mixture than protocells (100–150 nm in diameter) used to collect the images shown in **b–d**. Scale bar = 5 μm . **b–d**, Hyperspectral confocal fluorescence microscopy was employed to individually track the lipid and silica moieties of DOPC protocells (100–150 nm multimodal core), as well as the four surrogate cargos within the cytosol (purple) and nuclei (blue) of Hep3B cells as a function of time. **b**, Within 15 min of exposing Hep3B to protocells loaded with the multicomponent mixture, the lipid, silica and cargo moieties have a punctate appearance, indicating that protocells are localized within endosomes. **c**, Within 4 h, the H5WYG peptide promotes endosomal escape, thereby releasing the lipid, silica and cargos into the cytosol of the Hep3B cells. **d**, Within 12 h, calcein and the dsDNA oligonucleotide, both of which are modified with an NLS, become concentrated in the nucleus, whereas the RFP and quantum dots (not modified with an NLS) remain largely localized in the cytosol. Protocells used to collect the images shown in **b–d** have a high capacity for the multicomponent mixture: 10^{10} protocells encapsulate 425 μmol of calcein, 7.6 μmol of the dsDNA oligonucleotide, 945 nmol of RFP, and 1.98×10^{13} quantum dots. Scale bars = 20 μm .

sequence (NLS; ref. 45) become concentrated in the nucleus, because the NLS promotes transport through the nuclear pore complex. Figure 5d demonstrates that NLS-modified calcein and dsDNA become localized in the nuclei of Hep3B cells within 12 h, whereas RFP and quantum dots (not modified with the NLS) remain concentrated in the cytosol.

We have used the above sequence of events to deliver high payloads of various cytotoxic agents to HCC, including drugs and drug cocktails, siRNA cocktails (see Supplementary Figs S13 and S14) and protein toxins (see Supplementary Figs S15 and S16) without affecting the viability of hepatocytes and other control cells. Figure 6 compares the cargo capacity, time-dependent release characteristics and selective cytotoxicity of SP94-targeted protocells and liposomes loaded with the chemotherapeutic drug doxorubicin (DOX). Protocells, owing to the high surface area and porosity of their nanoporous cores, have a 1,000 times higher capacity for DOX than similarly sized liposomes (loaded through an ammonium phosphate gradient-based approach⁴⁶) and can be engineered to release nearly 90% of their encapsulated DOX in a bioactive form on endocytosis by HCC (see ‘Effective capacity’ in Fig. 6a, left axis). Additionally, DOPC protocells exhibit long-term stability when

maintained in a simulated body fluid (pH 7.4) at 37 °C, whereas DOPC liposomes leak 90% of their encapsulated DOX within 72 h and have a release profile comparable to that of the nanoporous core with no SLB. Thus, the fluid lipids that enable selective targeting at low peptide densities cannot be used in liposomal drug formulations, because premature release of encapsulated cargo results in undesired toxicity to non-cancerous cells. Stable formulations of liposomal drugs require the use of fully saturated, high- T_m lipids (for example 1,2-distearoyl-*sn*-glycero-3-phosphocholine (DSPC), $T_m = 55 \text{ }^\circ\text{C}$) and high concentrations of cholesterol, which act cooperatively to increase the lipid packing density and limit diffusion of the drug across the bilayer⁴⁷. Even the stability of ‘gold standard’ liposomal DOX (for example DSPC with 30 wt% cholesterol and 5 wt% PEG) remains limited, however, as up to 25% of the drug is released within 72 h when exposed to a simulated body fluid at 37 °C (see ‘DSPC liposomes’ in Fig. 6b).

Exposing protocells to a pH 5.0 buffer, which simulates the endosomal environment and destabilizes the SLB (see Supplementary Fig. S12), promotes rapid release of drugs loaded within the nanoporous core; DOPC protocells release 99% of their encapsulated DOX within 12 h (see Fig. 6c). DSPC and DOPC

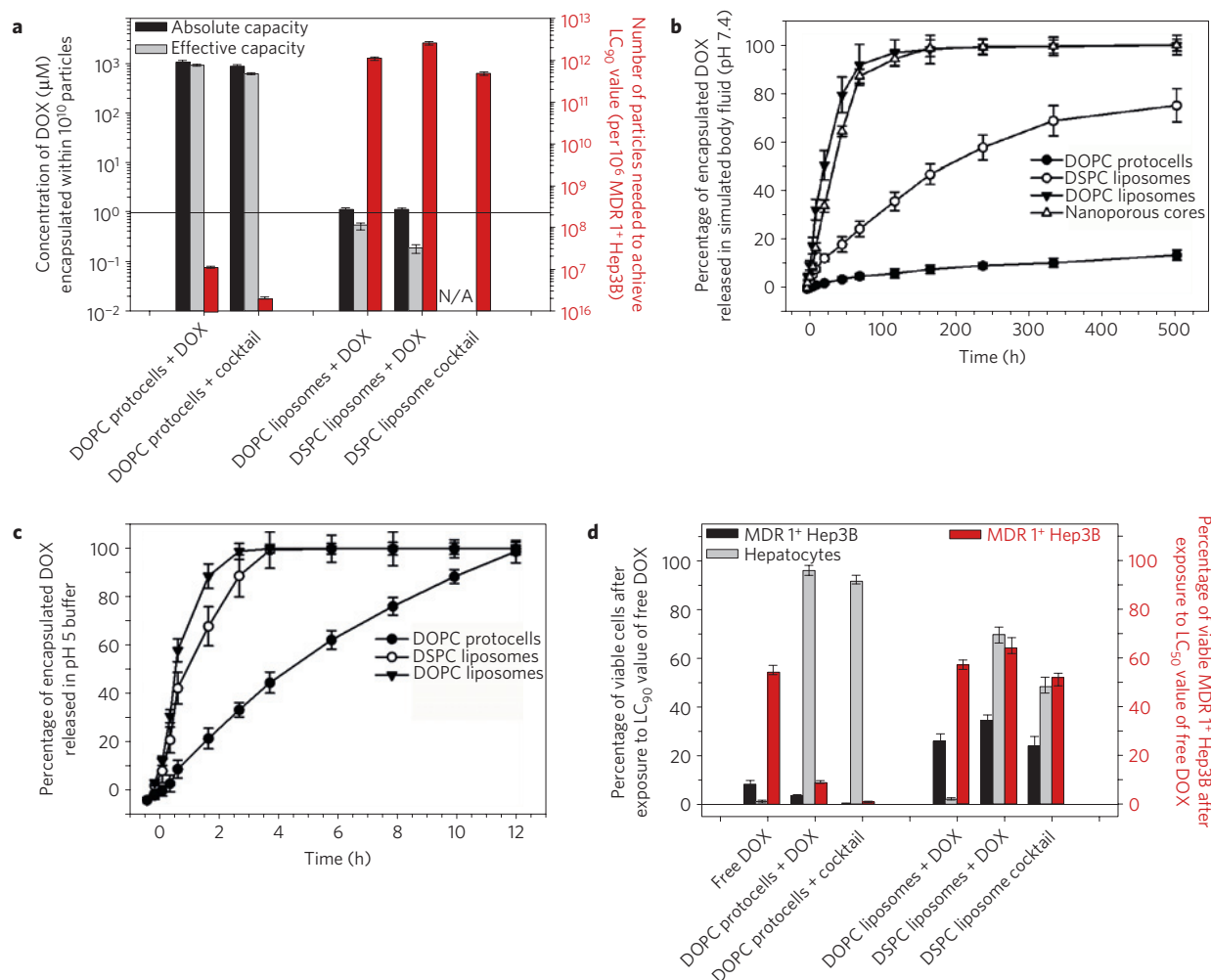


Figure 6 | Cargo capacity, time-dependent release profiles and concentration-dependent cytotoxicity of SP94-targeted protocells and liposomes that encapsulate chemotherapeutic drugs. **a**, Cargo capacity and cytotoxicity of protocells and liposomes loaded with DOX. Left axis: The absolute and effective capacities of DOPC protocells, DOPC liposomes and DSPC liposomes for DOX. Absolute capacity is defined as the concentration of DOX that can be physically encapsulated within 10^{10} particles, whereas effective capacity is the concentration of DOX that is released on endocytosis by Hep3B in a form capable of intercalating nuclear DNA. DOPC protocells, when loaded with a cocktail of DOX, 5-fluorouracil (5-FU) and cisplatin, retain their high absolute and effective capacities. The liposome cocktail is composed of equal volumes of DOX-loaded, 5-FU-loaded and cisplatin-loaded DSPC liposomes. DSPC liposomes that encapsulate 5-FU have an absolute capacity of 765 nM (per 10^{10} particles) and were prepared using the reverse-phase evaporation method described in ref. 52. DSPC liposomes that encapsulate cisplatin have an absolute capacity of 980 nM (per 10^{10} particles) and were prepared using the technique described in ref. 53. Right axis: The number of DOX-loaded protocells or liposomes that must be added to 10^6 MDR1⁺ Hep3B cells to kill 90% of the cells in the population (LC_{90}) within 24 h. **b**, The time-dependent release of DOX from DOPC protocells, DSPC liposomes, DOPC liposomes and nanoporous silica cores when exposed to a simulated body fluid (pH 7.4) at 37°C for 21 days. **c**, The time-dependent release of DOX from DOPC protocells, DSPC liposomes and DOPC liposomes when exposed to a pH 5 citric acid buffer at 37°C for 12 h. Acidic conditions, which mimic those of the endosome, destabilize the SLB and promote release of DOX from the protocell's nanoporous core. **d**, Left axis: The number of MDR1⁺ Hep3B and hepatocytes that remain viable after exposure to $9.6 \mu\text{M}$ of free DOX, protocell-encapsulated DOX or liposomal DOX for 24 h at 37°C . $9.6 \mu\text{M}$ is the LC_{90} value of free DOX when exposed to Hep3B with induced MDR (MDR1⁺ phenotype) and was, therefore, selected as the standardized drug concentration. Cells were exposed to drugs and drug-loaded nanocarriers for 24 h because the typical doubling time of HCC is 24–36 h. Right axis: The number of MDR1⁺ Hep3B that remain viable after exposure to $2.4 \mu\text{M}$ free DOX, protocell-encapsulated DOX or liposomal DOX for 24 h at 37°C ; $2.4 \mu\text{M}$ is the LC_{50} value of free DOX. Sytox Green nucleic acid stain and Alexa Fluor 647-labelled annexin V were used to distinguish viable (double-negative) from non-viable (single- or double-positive) cells. All error bars represent 95% confidence intervals (1.96σ) for $n = 3$.

liposomes release nearly all of their encapsulated DOX on exposure to a pH 5.0 buffer for 4 h (see Fig. 6c). Differences in absolute cargo capacities must be taken into account, however, to accurately compare the drug delivery capabilities of targeted protocells and liposomes. DOPC protocells release $\sim 50\%$ of their encapsulated DOX within 4 h, which corresponds to a drug concentration of nearly $500 \mu\text{M}$ when the protocell concentration is maintained at 10^{10} particles ml^{-1} . In comparison, 10^{10} liposomes release only $\sim 1 \mu\text{M}$ of DOX in the same period of time. It is important to

note that the DSPC liposomes referred to in Fig. 6 have a similar capacity for DOX ($\sim 1.1 \mu\text{M}$ per 10^{10} particles), which corresponds to a drug:lipid ratio of 0.113:1) to other PEGylated liposomal DOX formulations, including Doxil (drug:lipid ratio of 0.125:1; ref. 47).

The unique properties of drug-loaded DOPC protocells modified with a minimal number of targeting peptides solve the conundrum of simultaneously achieving high targeting specificity, high cytotoxicity to the target cell, and low collateral damage to non-cancerous cells. Figure 6a (right axis) plots the number

of DOX-loaded DOPC protocells, DSPC liposomes and DOPC liposomes needed to kill 90% of Hep3B (LC_{90}) with an induced MDR1 phenotype. We find that 10^5 fewer DOX-loaded protocells are necessary to achieve this LC_{90} value when compared with DOX-loaded DSPC or DOPC liposomes. Figure 6d (left axis) plots the percentage of Hep3B and hepatocytes that remain viable after exposure to either free DOX or to DOX encapsulated within DOPC protocells, DSPC liposomes or DOPC liposomes for 24 h at 37 °C; here the total DOX concentration was normalized to 9.6 μ M, which is the concentration of free DOX necessary to kill 90% of MDR1⁺ Hep3B within 24 h. We observe that DOX-loaded DOPC protocells maintain greater than 90% hepatocyte viability, while killing nearly 97% of MDR1⁺ Hep3B. In comparison, DOX-loaded DSPC and DOPC liposomes are less efficient at killing HCC and cause significant cytotoxicity to non-cancerous cells. Figure 6d (right axis) shows the number of MDR1⁺ Hep3B that remain viable after incubation with a lower concentration (2.3 μ M, the LC_{50} value of free DOX) of free DOX, DOX-loaded protocells or DOX-loaded liposomes. These data are included to clearly demonstrate the enhanced killing efficacy of DOX-loaded protocells when compared with both free DOX and DOX-loaded liposomes, an observation that is further supported by the fact that DOX-loaded protocells decrease the LC_{90} value of free DOX (9.6 μ M) to \sim 145 nM. We attribute the striking differences shown in Fig. 6a (right axis) and 6d to the 1,000 times higher capacity (Fig. 6a, left axis), the enhanced binding affinity (Fig. 4a) and the greater long-term stability (Fig. 6b) of DOPC protocells. These factors synergistically combine to provide dramatic improvements in selective cytotoxicity of cancer, while limiting undesired toxicity to normal hepatocytes. Protocells can, furthermore, be easily loaded with multicomponent cargos by simply soaking the nanoporous core in a solution of the desired cargos before fusion of the SLB. Figure 6a (right axis) and 6d show that, when loaded with a cocktail of DOX, 5-fluorouracil and cisplatin (a chemotherapeutic drug cocktail known to be particularly effective against drug-resistant HCC; ref. 48), as little as one SP94-targeted DOPC protocell is sufficient to kill a Hep3B cell with an induced MDR1 phenotype while maintaining more than 90% hepatocyte viability. Similar results cannot be achieved using DOPC and DSPC liposomes, because liposomes cannot be loaded with drug cocktails using strategies based on transmembrane pH gradients. A cocktail of DSPC liposomes that individually encapsulate DOX, 5-FU or cisplatin was employed as a control but failed to substantially improve on the selective cytotoxicity of DOX-loaded DSPC liposomes (see Fig. 6a,d).

We have demonstrated that targeted protocells possess the high specificity, enhanced cargo capacity and long-term stability necessary to deliver a variety of chemically disparate therapeutic and diagnostic agents to cancer cells with minimal nonspecific binding and toxicity to normal cells. We have, furthermore, shown that the nanoporous core can be adapted to release encapsulated cargo within 24 h or over the course of several weeks (see Supplementary Fig. S2), and that the SLB can be modified with a variety of ligands, including peptides, antibodies and glycoproteins, to promote specific affinity for a target cell (see section 2 in Supplementary Figures and Legends).

So far, no other nanoparticle-based delivery vehicle has been reported that possesses all of these attributes, making protocells the first example of a nanocarrier that simultaneously addresses the complex requirements of targeted, multicomponent delivery. Perhaps the most striking feature of protocells is their ability to deliver high concentrations of diverse cargos and 'cocktails' of chemically disparate components. For example, Supplementary Figs S13 and S14 report preliminary data regarding the killing efficacy of SP94-targeted protocells loaded with an siRNA cocktail that silences expression of epidermal growth factor receptor, vascular endothelial growth factor receptor-2 and platelet-derived growth

factor receptor- α . Protocells encapsulate 1,000 times more siRNA than similarly sized liposomes with the same bilayer composition and, when targeted with the SP94 peptide, induce apoptosis in 50% of Hep3B within 36 h without affecting the viability of hepatocytes. Another distinctive characteristic of protocells is that the enhanced fluidity and stability of the SLB support multivalent peptide recruitment to surface receptors expressed by the target cell, which suggests that displaying two or more types of ligand on the protocell surface might enable complex binding interactions. We expect, therefore, that modifying the protocell SLB with ligand(s) that bind to surface receptor(s) uniquely or overexpressed by the target cell along with a ligand that promotes internalization (for example the octaarginine peptide, which stimulates macropinocytosis⁴⁹) would enable both selective targeting and intracellular delivery for cancers where cell-specific receptors are not normally endocytosed.

Methods

Nanoporous silica particles were synthesized and characterized as described previously^{26,50} and as detailed in Supplementary Fig. S1 and the Supplementary Methods section. Particles larger than \sim 150-nm in diameter were removed by differential centrifugation or size-exclusion chromatography (see Supplementary Fig. S1a,d). Protocells were formed by fusing \sim 120 nm liposomes to the nanoporous core as reported previously^{23–25}, and the composition of the SLB was optimized to reduce nonspecific binding associated with cationic and, to a lesser extent, anionic lipids⁵¹ (see Supplementary Fig. S5). Zwitterionic lipids (DOPC or DPPC) with 5 wt% PE (DOPE or DPPE, respectively), 5 wt% PEG-2000 PE (18:0 or 16:0, respectively) and 30 wt% cholesterol were used in all further studies; PEGylated lipids were incorporated into the liposomes used for fusion and are, therefore, expected to be present on both the inner and outer leaflets of the SLB. The size of the nanoporous core was also optimized to attain a balance between achievable cargo capacity and the rate of protocell internalization (see Supplementary Fig. S9); nanoparticles 100–150 nm in diameter were employed in the delivery of drugs, drug cocktails, siRNA cocktails and protein toxins. The nanoporous cores were soaked in a 10 mM solution of cargo(s) for 1–12 h before liposome fusion; individual components of the surrogate cargo mixture (Fig. 5) and the drug cocktail (Fig. 6) were loaded into nanoporous cores simultaneously (as opposed to sequentially). The rates of cargo release were optimized by incorporating various percentages of AEPTMS, an amine-containing silane, into the sol used to form nanoporous cores (see Supplementary Fig. S2). Particles containing 15 wt% AEPTMS were used to deliver drugs and drug cocktails (Fig. 6), whereas particles containing 20 wt% AEPTMS were used to deliver the multicomponent mixture (Fig. 5), the siRNA cocktail (Supplementary Fig. S13 and 14) and diphtheria toxin A-chain (Supplementary Figs S15 and S16).

Received 17 May 2010; accepted 24 February 2011;
published online 17 April 2011

References

- Peer, D. *et al.* Nanocarriers as an emerging platform for cancer therapy. *Nature Nanotech.* **2**, 751–760 (2007).
- Wagner, V., Dullaart, A., Bock, A.-K. & Zwick, A. The emerging nanomedicine landscape. *Nature Biotechnol.* **24**, 1211–1217 (2006).
- Nel, A. E. *et al.* Understanding biophysicochemical interactions at the nano–bio interface. *Nature Mater.* **8**, 543–557 (2009).
- Ferrari, M. Cancer nanotechnology: Opportunities and challenges. *Nature Rev. Cancer* **5**, 161–171 (2005).
- Maeda, H., Wu, J., Sawa, T., Matsumura, Y. & Hori, K. Tumor vascular permeability and the EPR effect in macromolecular therapeutics: A review. *J. Control. Release* **65**, 271–284 (2000).
- Matsumura, Y. & Maeda, H. A new concept for macromolecular therapeutics in cancer chemotherapy: Mechanism of tumoritropic accumulation of proteins and the antitumor agent SMANCS. *Cancer Res.* **46**, 6387–6392 (1986).
- Gottesman, M. M., Fojo, T. & Bates, S. E. Multidrug resistance in cancer: Role of ATP-dependent transporters. *Nature Rev. Cancer* **2**, 48–58 (2002).
- Kohlschütter, J., Michelfelder, S. & Trepel, M. Drug delivery in acute myeloid leukemia. *Expert Opin. Drug Deliv.* **5**, 653–663 (2008).
- Torchilin, V. P. Recent advances with liposomes as pharmaceutical carriers. *Nature Rev. Drug Discov.* **4**, 145–160 (2005).
- Rai, P. *et al.* Statistical pattern matching facilitates the design of polyvalent inhibitors of anthrax and cholera toxins. *Nature Biotechnol.* **24**, 582–586 (2006).
- Jiang, W., Kim, B. Y. S., Rutka, J. T. & Chan, W. C. W. Nanoparticle-mediated cellular response is size-dependent. *Nature Nanotech.* **3**, 145–150 (2008).
- Pastan, I., Hassan, R., FitzGerald, D. J. & Kreitman, R. J. Immunotoxin therapy of cancer. *Nature Rev. Cancer* **6**, 559–565 (2006).
- Ferrari, M. Nanogeometry: Beyond drug delivery. *Nature Nanotech.* **3**, 131–132 (2008).

14. Giri, S., Trewyn, B. G., Stellmaker, M. P. & Lin, V. S. Y. Stimuli-responsive controlled-release delivery system based on mesoporous silica nanorods capped with magnetic nanoparticles. *Angew. Chem. Int. Ed.* **44**, 5038–5044 (2005).
15. Lai, C.-Y. *et al.* A mesoporous silica nanosphere-based carrier system with chemically removable CdS nanoparticle caps for stimuli-responsive controlled release of neurotransmitters and drug molecules. *J. Am. Chem. Soc.* **125**, 4451–4459 (2003).
16. Liong, M. *et al.* Multifunctional inorganic nanoparticles for imaging, targeting, and drug delivery. *ACS Nano* **2**, 889–896 (2008).
17. Nguyen, T. D. *et al.* A reversible molecular valve. *Proc. Natl Acad. Sci. USA* **102**, 10029–10034 (2005).
18. Patel, K. *et al.* Enzyme-responsive snap-top covered silica nanocontainers. *J. Am. Chem. Soc.* **130**, 2382–2383 (2008).
19. Vallet-Regí, M., Balas, F. & Arcos, D. Mesoporous materials for drug delivery. *Angew. Chem. Int. Ed.* **46**, 7548–7558 (2007).
20. Davis, M. E., Chen, Z. & Shin, D. M. Nanoparticle therapeutics: An emerging treatment modality for cancer. *Nature Rev. Drug Discov.* **7**, 771–782 (2008).
21. Gordon, A. N. *et al.* Recurrent epithelial ovarian carcinoma: A randomized phase III study of pegylated liposomal doxorubicin versus topotecan. *J. Clin. Oncol.* **19**, 3312–3322 (2001).
22. Peer, D., Zhu, P., Carman, C. V., Lieberman, J. & Shimaoka, M. Selective gene silencing in activated leukocytes by targeting siRNAs to the integrin lymphocyte function-associated antigen-1. *Proc. Natl Acad. Sci. USA* **104**, 4095–4100 (2007).
23. Liu, J. W., Jiang, X. M., Ashley, C. & Brinker, C. J. Electrostatically mediated liposome fusion and lipid exchange with a nanoparticle-supported bilayer for control of surface charge, drug containment, and delivery. *J. Am. Chem. Soc.* **131**, 7567–7569 (2009).
24. Liu, J. W., Stace-Naughton, A. & Brinker, C. J. Silica nanoparticle supported lipid bilayers for gene delivery. *Chem. Commun.* 5100–5102 (2009).
25. Liu, J. W., Stace-Naughton, A., Jiang, X. M. & Brinker, C. J. Porous nanoparticle supported lipid bilayers (protocells) as delivery vehicles. *J. Am. Chem. Soc.* **131**, 1354–1355 (2009).
26. Lu, Y. F. *et al.* Aerosol-assisted self-assembly of mesostructured spherical nanoparticles. *Nature* **398**, 223–226 (1999).
27. Evans, E. Entropy-driven tension in vesicle membranes and unbinding of adherent vesicles. *Langmuir* **7**, 1900–1908 (1991).
28. Komura, S., Shimokawa, N. & Andelman, D. Tension-induced morphological transition in mixed lipid bilayers. *Langmuir* **22**, 6771–6774 (2006).
29. Lipowsky, R. The conformation of membranes. *Nature* **349**, 475–481 (1991).
30. Mutz, M. & Helfrich, W. Unbinding transition of a biological model membrane. *Phys. Rev. Lett.* **62**, 2881–2884 (1989).
31. Netz, R. R. & Lipowsky, R. Stacks of fluid membranes under pressure and tension. *Europhys. Lett.* **29**, 345–350 (1995).
32. Swain, P. S. & Andelman, D. Supported membranes on chemically structured and rough surfaces. *Phys. Rev. E* **63**, 051911 (2001).
33. Bothun, G. D., Knutson, B. L., Strobel, H. J. & Nokes, S. E. Liposome fluidization and melting point depression by pressurized CO₂ determined by fluorescence anisotropy. *Langmuir* **21**, 530–536 (2004).
34. Doshi, D. A. *et al.* Neutron reflectivity study of lipid membranes assembled on ordered nanocomposite and nanoporous silica thin films. *Langmuir* **21**, 2865–2870 (2005).
35. Daillant, J. *et al.* Structure and fluctuations of a single floating lipid bilayer. *Proc. Natl Acad. Sci. USA* **102**, 11639–11644 (2005).
36. Malaquin, L., Charitat, T. & Daillant, J. Supported bilayers: Combined specular and diffuse X-ray scattering. *Eur. Phys. J. E* **31**, 285–301 (2010).
37. Huang, S.-C. J. *et al.* Formation, stability, and mobility of one-dimensional lipid bilayers on polysilicon nanowires. *Nano Lett.* **7**, 3355–3359 (2007).
38. Swain, P. S. & Andelman, D. The influence of substrate structure on membrane adhesion. *Langmuir* **15**, 8902–8914 (1999).
39. Lo, A., Lin, C. T. & Wu, H. C. Hepatocellular carcinoma cell-specific peptide ligand for targeted drug delivery. *Mol. Cancer Therapeut.* **7**, 579–589 (2008).
40. Chen, Z. *et al.* DNA translocation through an array of kinked nanopores. *Nature Mater.* **9**, 667–675 (2010).
41. Lu, Y. F. *et al.* Continuous formation of supported cubic and hexagonal mesoporous films by sol gel dip-coating. *Nature* **389**, 364–368 (1997).
42. Goren, D. *et al.* Nuclear delivery of doxorubicin via folate-targeted liposomes with bypass of multidrug-resistance efflux pump. *Clin. Cancer Res.* **6**, 1949–1957 (2000).
43. Midoux, P., Kichler, A., Boutin, V., Maurizot, J.-C. & Monsigny, M. Membrane permeabilization and efficient gene transfer by a peptide containing several histidines. *Bioconj. Chem.* **9**, 260–267 (1998).
44. Behr, J. P. The proton sponge: A trick to enter cells the viruses did not exploit. *CHIMIA Int. J. Chem.* **51**, 34–36 (1997).
45. Subramanian, A., Ranganathan, P. & Diamond, S. L. Nuclear targeting peptide scaffolds for lipofection of nondividing mammalian cells. *Nature Biotechnol.* **17**, 873–877 (1999).
46. Fritze, A., Hens, F., Kimpfler, A., Schubert, R. & Peschka-Süss, R. Remote loading of doxorubicin into liposomes driven by a transmembrane phosphate gradient. *Biochim. Biophys. Acta Biomembr.* **1758**, 1633–1640 (2006).
47. Drummond, D. C., Meyer, O., Hong, K., Kirpotin, D. B. & Papahadjopoulos, D. Optimizing liposomes for delivery of chemotherapeutic agents to solid tumors. *Pharmacol. Rev.* **51**, 691–744 (1999).
48. Lee, J. O. *et al.* Combination chemotherapy with capecitabine and cisplatin for patients with metastatic hepatocellular carcinoma. *Ann. Oncol.* **20**, 1402–1407 (2009).
49. Khalil, I. A., Kogure, K. & Futaki, S. High density of octaarginine stimulates macropinocytosis leading to efficient intracellular trafficking for gene expression. *J. Biol. Chem.* **281**, 3544–3551 (2006).
50. Carroll, N. J., Pylypenko, S., Atanassov, P. B. & Petsev, D. N. Microparticles with bimodal nanoporosity derived by microemulsion templating. *Langmuir* **25**, 13540–13544 (2009).
51. Xia, T. *et al.* Comparison of the mechanism of toxicity of zinc oxide and cerium oxide nanoparticles based on dissolution and oxidative stress properties. *ACS Nano* **2**, 2121–2134 (2008).
52. Elorza, B., Elorza, M. A., Frutos, G. & Chantres, J. R. Characterization of 5-fluorouracil loaded liposomes prepared by reverse-phase evaporation or freezing–thawing extrusion methods: Study of drug release. *Biochim. et Biophys. Acta* **1153**, 135–142 (1993).
53. Peleg-Shulman, T., Gibson, D., Cohen, R., Abra, R. & Barenholz, Y. Characterization of sterically stabilized cisplatin liposomes by nuclear magnetic resonance. *Biochim. Biophys. Acta* **1510**, 278–291 (2001).

Acknowledgements

This work was supported by the NIH/Roadmap for Medical Research under grant PHS 2 PN2 EY016570B; NCI Cancer Nanotechnology Platform Partnership grant 1U01CA151792-01; the Air Force Office of Scientific Research grant FA 9550-07-1-0054/9550-10-1-0054; the US Department of Energy, Office of Basic Energy Sciences, Division of Materials Sciences and Engineering; the Sandia National Laboratories' Laboratory Directed Research and Development (LDRD) programme; the President Harry S. Truman Fellowship in National Security Science and Engineering at Sandia National Laboratories (C.E.A.); the UCLA Center for Nanobiology and Predictive Toxicology (NIEHS grant 1U19ES019528-01) and the NSF ERC Center for Environmental Implications of Nanotechnology at UCLA (NSF:EF-0820117). C.E.A. was supported by IGERT Fellowship Grant NSF DGE-0504276, and E.C.C. and N.J.C. were supported by NSF IGERT grant DGE- 0549500. T.N.H. was supported by NSF Nanoscience and Microsystems REU program (grant DMR-0649132) at the University of New Mexico Center for Micro-Engineered Materials. N.J.C. and D.N.P. were supported by NSF PREM/DMR 0611616. R. Lee provided guidance for imaging protocols and FRAP experiments, M. Aragon created schematic diagrams, R. Sewell carried out nitrogen sorption experiments and Y.-B. Jiang carried out TEM imaging. Cryogenic TEM was carried out at Baylor College of Medicine (Houston, TX) by C. Jia-Yin Fu, H. Khant and W. Chiu. Some images in this paper were generated in the University of New Mexico Cancer Center Fluorescence Microscopy Facility, supported by NCRR, NSF and NCI as detailed at <http://hsc.unm.edu/crtc/microscopy/Facility.html>. Data were generated in the Flow Cytometry Shared Resource Center supported by the University of New Mexico Health Sciences Center and the University of New Mexico Cancer Center. Sandia is a multiprogramme laboratory operated by Sandia Corporation, a wholly owned subsidiary of Lockheed Martin Company, for the US Department of Energy's National Nuclear Security Administration under contract DE-AC04-94AL85000.

Author contributions

C.E.A. engineered protocells for targeted delivery, carried out most experiments, analysed data and wrote the manuscript; E.C.C. assisted with experiment coordination, data analysis and manuscript preparation; G.K.P. carried out confocal fluorescence microscopy imaging; D.P. synthesized and characterized multimodal particles; P.A.B. carried out FRAP experiments; T.N.H. assisted with DOX capacity and release studies; J.L. contributed to the development of the original protocol construct; N.J.C. developed the emulsion processing necessary to synthesize multimodal particles; B.P. and M.B.C. carried out flow cytometry experiments; X.J. synthesized unimodal particles; D.R.D. carried out small-angle neutron scattering experiments and analysed nitrogen sorption data; D.N.P. supervised development of the multimodal particles; D.G.E. supervised FRAP experiments; A.N.P. suggested the FRAP experiment and aided in its interpretation; P.N.D., C.L.W., B.C., W.W. and D.S.P. provided intellectual oversight for delivery experiments involving drugs, siRNA and protein toxins; C.J.B. conceived of the protocol construct, provided overall intellectual guidance, carried out final edits of the manuscript and is principal investigator of the main supporting grants.

Additional information

The authors declare no competing financial interests. Supplementary information accompanies this paper on www.nature.com/naturematerials. Reprints and permissions information is available online at <http://npg.nature.com/reprintsandpermissions>. Correspondence and requests for materials should be addressed to C.E.A. or C.J.B.